Lattice Boltzmann Finite Volume Formulation with Improved Stability

A. Zarghami[1,*], M. J. Maghrebi[2], J. Ghasemi[3] and S. Ubertini[4]

[1] *Department of Mechanical Engineering, Shahrood University of Technology, Shahrood, Iran.*
[2] *Department of Mechanical Engineering, Ferdowsi University of Mashhad, Mashhad, Iran.*
[3] *Faculty of Engineering, Zanjan University, Zanjan, Iran.*
[4] *Department of Technologies, University of Naples "Parthenope", Naples, Italy.*

Abstract. The most severe limitation of the standard Lattice Boltzmann Method is the use of uniform Cartesian grids especially when there is a need for high resolutions near the body or the walls. Among the recent advances in lattice Boltzmann research to handle complex geometries, a particularly remarkable option is represented by changing the solution procedure from the original "stream and collide" to a finite volume technique. However, most of the presented schemes have stability problems. This paper presents a stable and accurate finite-volume lattice Boltzmann formulation based on a cell-centred scheme. To enhance stability, upwind second order pressure biasing factors are used as flux correctors on a D2Q9 lattice. The resulting model has been tested against a uniform flow past a cylinder and typical free shear flow problems at low and moderate Reynolds numbers: boundary layer, mixing layer and plane jet flows. The numerical results show a very good accuracy and agreement with the exact solution of the Navier-Stokes equation and previous numerical results and/or experimental data. Results in self-similar coordinates are also investigated and show that the time-averaged statistics for velocity and vorticity express self-similarity at low Reynolds numbers. Furthermore, the scheme is applied to simulate the flow around circular cylinder and the Reynolds number range is chosen in such a way that the flow is time dependent. The agreement of the numerical results with previous results is satisfactory.

PACS: 47.20.Ky, 47.11.Df

Key words: Lattice Boltzmann equation, finite volume, stability, cell-centered scheme, free shear flows.

---

*Corresponding author. *Email addresses:* `ahad.zarghami@gmail.com` (A. Zarghami), `mjmaghrebi@um.ac.ir` (M. J. Maghrebi), `j.ghasemi@znu.ac.ir` (J. Ghasemi), `Stefano.ubertini@uniparthenope.it` (S. Ubertini)

1 Introduction

Computational fluid dynamics, in its conventional meaning, computes pertinent flow fields in terms of velocity, density, pressure and temperature by numerically solving the Navier-Stokes equations in time and space. At the turn of the 1980s, the Lattice Boltzmann Method (LBM) has been proposed as an alternative approach to solve fluid dynamics problems. The main philosophy of the LBM is to compute the physical reality of a flow field through a microscopic kinetic approach that preserves the hydrodynamic conservation laws [1,2]. As a different approach from the conventional computational fluid dynamics, the LBM, initially developed from its predecessor the Lattice Gas Automata (LGA) [3], has rapidly evolved into a self-standing research subject and has proven to be an efficient tool for simulating a variety of nontrivial transport phenomena and fluid dynamics problems such as hydrodynamics in porous media, multi-phase or multi-component flows, reactive chemical flow, magneto-hydrodynamics, etc. [4–8]. Because of the broad scope and great potential of its applications, the LBE method has been viewed not only as a novel technique, but also as a new and general approach in the spirit of kinetic theory for the study of complex systems.

The kinetic nature of the LBE leads to several advantages. Pressure field and stress tensor are locally available, with no need of solving any (expensive) Poisson problem. Moreover, non-linearities are local (quadratic dependence of the local equilibrium on the flow field) and the non-localities are linear because advection proceeds along constant, straight lines defined by the discrete particle speeds. This is a very useful property, not shared by the Navier-Stokes equations, in which non-linearity and non-locality come together into the same term, that is, the fluid moves its own momentum along a space-time changing direction defined by the flow speed itself. Finally, the LBE method, the constitutive relations emerge as a result of proper modeling of inter-particle potentials. Several references are available to obtain an entry to the theory and methodology of LBE [9,10].

One of the crucial ingredients which concurs to the LB efficiency is that particles live on a discrete lattice, thus greatly simplifying the dynamics and the bookkeeping of the method. However, this leads to geometrical stiffness, resulting into a uniform spatial grid. This represents a very severe limitation for many practical applications, particularly for multiscale-type calculations, where selective distribution of the computational degrees of freedom in the "hot" regions is necessary.

Such difficulty may be overcome by decoupling the numerical mesh from the lattice structure, and taking recourse to, one of finite difference or finite element approaches. He et al. [11] proposed an algorithm that adds an interpolation step to the standard LBM and Succi et al. [12] were the first to propose a finite-volume formulation of the lattice Boltzmann equation. Both of these methods require a topologically structured mesh, though the grid points do not have to form a square lattice. Peng et al. [13,14] proposed a cell-vertex finite volume scheme, which was further developed by Ubertini et al. [15]. This method allows for an arbitrary decomposition of the computational domain into triangular or quadrilateral elements, with otherwise no structural limitations for the mesh.

However, the proposed method has several drawbacks with respect to numerical stability and improved stability is needed [16].

The present work is aimed at making progress in the direction of developing a stable finite volume formulation of the LBE with single time relaxation to equilibrium. A cell-centered finite volume approach is used for space discretization and numerical stability is improved by employing second order upwind biasing factors. The performance of the formulation is systematically investigated by simulating three free shear flows, namely 1-boundary layer, 2-mixing layer and 3-plane jet flow. For each of these flows, the present scheme is validated with the exact solution of the Navier-Stokes equation and literature results. It is shown that the scheme has very high accuracy and is robust and accurate for the different test problems studied.

The paper is organized as follows. In Section 2 a short summary of the discrete LB equation and the proposed cell-centered finite-volume scheme are discussed. In Section 3 viscosity calculation and error analysis are performed through the simulation of a Taylor vortex flow. Sections 4 and 5 contain simulation results of free shear flows and uniform flow past a cylinder, respectively. Finally, concluding remarks are presented.

2 The numerical model

2.1 Discrete Boltzmann equation

The lattice Boltzmann equation can be directly derived from the Boltzmann equation by discretization in phase space without borrowing the concept of particles jumping from site to site as in the LGA model [3]. A popular kinetic model is the single relaxation time approximation, the so-called Bhatnagar-Gross-Krook (BGK) model [1]

$$\frac{\partial f_i}{\partial t} + \vec{v}_i \cdot \nabla f_i = -\frac{1}{\tau}\left(f_i - f_i^{eq}\right), \qquad i=1,\cdots,n, \tag{2.1}$$

where n is the number of different velocities in the model, f^{eq} is the particle equilibrium distribution function (the Maxwell-Boltzmann distribution function) associated with motion along the ith direction in velocity space, $\vec{v}_i$ the velocity in the ith direction, τ is the relaxation time and the right hand side of the equation is the collision operator.

In the LBM, only a small set of discrete velocities are used to approximate the Boltzmann kinetics of the continuum velocity. So, to solve for f numerically, Eq. (2.1) is first discretized in the phase space using a finite set of velocities without violating the conservation laws. It should be pointed out that in the phase space the space variable **x** and the velocity variable **v** are independent [17]. In the present work we shall refer to the nine velocities model denoted as D2Q9, in which the nine discrete velocities are defined as follows:

$$\mathbf{v} = \begin{cases} (0,0), & i=0, \\ \left[\cos\left(\frac{i-1}{2}\pi\right),\sin\left(\frac{i-1}{2}\pi\right)\right]c, & i=1,2,3,4, \\ \sqrt{2}\left[\cos\left(\frac{i-5}{2}+\frac{1}{4}\right)\pi,\sin\left(\frac{i-5}{2}+\frac{1}{4}\right)\pi\right]c, & i=5,6,7,8, \end{cases} \tag{2.2}$$

where c is an arbitrary constant related to speed of sound by $c_s = c/\sqrt{3}$, see [17]. The equilibrium distribution for D2Q9 model is given by:

$$f_i^{eq}(\vec{x},t) = w_i \rho \left[c_1 + c_2(\vec{v}_i \cdot \mathbf{u}) + c_3(\vec{v}_i \cdot \mathbf{u})^2 + c_4(\mathbf{u} \cdot \mathbf{u}) \right], \tag{2.3}$$

where $c_1 = 1$, $c_2 = 1/2c_s^2$, $c_3 = 1/2c_s^4$, $c_4 = -1/2c_s^2$ and also $\rho = \sum_i f_i$ and $\rho \mathbf{u} = \sum_i f_i \vec{v}_i$ are the macroscopic mass density and momentum density respectively, and w_i is the weighting factor and equals $4/9$ for $i = 0$, $1/9$ for $i = 1-4$ and $1/36$ for $i = 5-8$. Note that the corresponding kinematic shear viscosity is related to the relaxation time by $v = c_s^2 \tau$ and macroscopic pressure is given by $p = c_s^2 \rho$, see [13–19].

2.2 Cell-centered finite volume scheme

The approach to numerically solve Eq. (2.1) is a cell-centred finite-volume scheme based on a space discretization into quadrilateral elements (see Fig. 1). For sake of simplicity the scheme is illustrated for a structured grid, but the method could be easily extended to unstructured grids. According to Fig. 1, the integration of the first term of the left-hand side of Eq. (2.1) is performed as follows:

$$\int_{abcd} \frac{\partial f_i}{\partial t} dA \approx \left[\frac{\partial f_i}{\partial t} \right]_{I,J} \cdot A_{I,J}, \tag{2.4}$$

where $A_{I,J}$ is the area of $abcd$. In the above equation, f_i is assumed to be constant over the area $abcd$, thus avoiding a set of equations to be solved. This is a common practice in the finite volume methods [14].

A standard integration of the second term of the left-hand side of Eq. (2.1) gives the flux associated to the streaming operator of the ith particle distribution function through
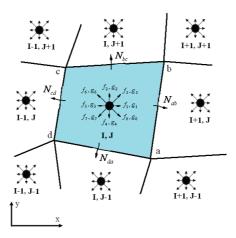

Figure 1: Schematic of the FV discretization with cell-centered lattice.

the four edges *ab*, *bc*, *cd* and *da*:

$$\int_{abcd} v_i \cdot \nabla f_i dA = \int_{abcd} \left\{ v_{ix} \frac{\partial f_i}{\partial x} + v_{iy} \frac{\partial f_i}{\partial y} \right\} dA. \tag{2.5}$$

As v_{ix} and v_{iy} are constant, the following equation is obtained after applying the Green's theorem:

$$\int_{abcd} v_i \cdot \nabla f_i dA = \int_{abcd} \left\{ \frac{\partial (v_{ix} \cdot f_i)}{\partial x} + \frac{\partial (f_i \cdot v_{iy})}{\partial y} \right\} dxdy = \oint_{around\ I,J} (v_{ix} f_i dy - v_{iy} f_i dx)$$

$$\approx \frac{[f_i]_{I,J} + [f_i]_{I+1,J}}{2} v_i \cdot N_{ab} + \frac{[f_i]_{I-1,J} + [f_i]_{I,J}}{2} v_i \cdot N_{bc}$$

$$+ \frac{[f_i]_{I,J} + [f_i]_{I,J+1}}{2} v_i \cdot N_{cd} + \frac{[f_i]_{I,J-1} + [f_i]_{I,J}}{2} v_i \cdot N_{da}. \tag{2.6}$$

In the above equation $N_k = \left(\Delta y \vec{i} - \Delta x \vec{j} \right)_k$ is the outward unit vector normal to the edge and $k = ab, bc, cd, da$. This formulation is named flux averaging scheme which would diverge if the flux term is weak [20].

   This could be avoided by using the divergence theorem and applying an upwind scheme. In this case the integration of the second term of the left-hand side of Eq. (2.1) results as follows [17]:

$$\int_{abcd} v_i \cdot \nabla f_i dA = \int_{abcd} \left[\frac{\partial (\vec{v}_{ix} \cdot f_i)}{\partial x} + \frac{\partial (\vec{v}_{iy} \cdot f_i)}{\partial y} \right] dxdy$$

$$= \begin{cases} [f_i]_{I,J} v_i \cdot N_{ab}, & \text{if } v_i \cdot N_{ab} \geq 0 \\ [f_i]_{I+1,J} v_i \cdot N_{ab}, & \text{if } v_i \cdot N_{ab} < 0 \end{cases} + \begin{cases} [f_i]_{I,J} v_i \cdot N_{bc}, & \text{if } v_i \cdot N_{bc} \geq 0 \\ [f_i]_{I,J+1} v_i \cdot N_{bc}, & \text{if } v_i \cdot N_{bc} < 0 \end{cases}$$

$$+ \begin{cases} [f_i]_{I,J} v_i \cdot N_{cd}, & \text{if } v_i \cdot N_{cd} \geq 0 \\ [f_i]_{I-1,J} v_i \cdot N_{cd}, & \text{if } v_i \cdot N_{cd} < 0 \end{cases} + \begin{cases} [f_i]_{I,J} v_i \cdot N_{da}, & \text{if } v_i \cdot N_{da} \geq 0 \\ [f_i]_{I,J-1} v_i \cdot N_{da}, & \text{if } v_i \cdot N_{da} < 0 \end{cases}$$

$$\approx \sum_k \vec{v}_i \cdot N_k (f_i)_k. \tag{2.7}$$

Now, the following second order pressure-based biasing factors are employed in the convective fluxes of Eq. (2.1):

$$\xi_{ab-Left} = \frac{p_{I-1,J}}{p_{I-1,J} + p_{I,J}}, \qquad \xi_{ab-Right} = \frac{p_{I,J}}{p_{I,J} + p_{I+1,J}} \rightarrow \xi_{ab} = \frac{\xi_{ab-Left} + \xi_{ab-Right}}{2}, \tag{2.8a}$$

$$\xi_{bc-Bottom} = \frac{p_{I,J-1}}{p_{I,J} + p_{I,J-1}}, \quad \xi_{bc-Top} = \frac{p_{I,J}}{p_{I,J+1} + p_{I,J}} \rightarrow \xi_{bc} = \frac{\xi_{bc-Bottom} + \xi_{bc-Top}}{2}, \tag{2.8b}$$

$$\xi_{cd-Right} = \frac{p_{I+1,J}}{p_{I,J} + p_{I+1,J}}, \quad \xi_{cd-Left} = \frac{p_{I,J}}{p_{I,J} + p_{I-1,J}} \rightarrow \xi_{cd} = \frac{\xi_{cd-Right} + \xi_{cd-Left}}{2}, \tag{2.8c}$$

$$\xi_{da-Top} = \frac{p_{I,J}}{p_{I,J} + p_{I,J+1}}, \qquad \xi_{da-Bottom} = \frac{p_{I,J}}{p_{I,J} + p_{I,J-1}} \rightarrow \xi_{da} = \frac{\xi_{da-Top} + \xi_{da-Bottom}}{2}. \tag{2.8d}$$

The idea of introducing these factors to improve numerical stability without adding artificial viscosity is related to the fact that the macroscopic pressure, p, acts as a driving force for the flow between the two cells. So, according to above relations, the convective fluxes may be written as follows [21]:

$$S_i = \int \vec{v}_i \cdot \nabla f_i \, dA \approx \vec{v}_i \cdot N_{ab} \left(\xi_{ab}[f_i]_{I,J} + (1 - \xi_{ab})[f_i]_{I+1,J} \right)$$
$$+ \vec{v}_i \cdot N_{bc} \left(\xi_{bc}[f_i]_{I,J} + (1 - \xi_{bc})[f_i]_{I,J+1} \right) + \vec{v}_i \cdot N_{cd} \left(\xi_{cd}[f_i]_{I,J} + (1 - \xi_{cd})[f_i]_{I-1,J} \right)$$
$$+ \vec{v}_i \cdot N_{da} \left(\xi_{da}[f_i]_{I,J} + (1 - \xi_{da})[f_i]_{I,J-1} \right). \tag{2.9}$$

The heuristic meaning of these coefficients is to enhance transport downhill the pressure gradient and reduce it uphill. Assuming a linear behavior of f_i, f_i^{eq} within internal cells, the integration of the collision term (right-side term of Eq. (2.1)) is performed through the following formulation:

$$Q_i = -\int_{abcd} \frac{1}{\tau} (f_i - f_i^{eq}) \, dA = -\frac{A_{I,J}}{\tau} \left[\frac{1}{4}[f_i^{ne}]_{I,J} + \frac{1}{8} \left([f_i^{ne}]_{I+1,J} + [f_i^{ne}]_{I,J+1} + [f_i^{ne}]_{I-1,J} \right. \right.$$
$$\left. + [f_i^{ne}]_{I,J-1} \right) + \frac{1}{16} \left([f_i^{ne}]_{I+1,J-1} + [f_i^{ne}]_{I+1,J+1} + [f_i^{ne}]_{I-1,J+1} + [f_i^{ne}]_{I-1,J-1} \right) \right], \tag{2.10}$$

where $f_i^{ne} = f_i - f_i^{eq}$ is the non-equilibrium component of the distribution function. Note that the integration of the collision terms in boundary cells takes the following form:

$$-\int_{abcd} \frac{1}{\tau} f_i^{ne} \, dA = -\frac{A_{I,J}}{\tau} \left[(f_i)_{I,J} - (f_i^{eq})_{I,J} \right]. \tag{2.11}$$

As we know truncation or round-off causes error in numerical solution of partial differential equations. So, the solution may go unstable in typical cases (such as flows with strong gradients) unless artificial dissipation is explicitly added to the calculation. Note that artificial dissipation is the direct result of even order derivatives in modified equation [22]. So, in flux modeling, especially at high Reynolds numbers or in the presence of strong gradients, the addition of artificial dissipation is inevitable to perform a stable simulation. Therefore, in order to damp out spurious oscillations the fourth-order artificial dissipation takes the following form:

$$\left[D^{(4)} f_i \right]_{I,J} = \varepsilon_x \cdot (\nabla \Delta)_x^2 \cdot [f_i]_{I,J} + \varepsilon_y \cdot (\nabla \Delta)_y^2 \cdot [f_i]_{I,J}, \tag{2.12}$$

where ε_x and ε_y are damping factors in x and y directions, respectively and the integration over each cell is the sum of flux and collision contributions in the time updating. These damping factors were adjusted to achieve desired numerical stability and convergence. In Eq. (2.12), the fourth-order gradient operator (Nabla-Delta) was discretized in x and y directions as follows:

$$(\nabla \Delta)_x^2 \cdot [f_i]_{I,J} = [f_i]_{I+2,J} - 4[f_i]_{I+1,J} + 6[f_i]_{I,J} - 4[f_i]_{I-1,J} + [f_i]_{I-2,J}, \tag{2.13a}$$
$$(\nabla \Delta)_y^2 \cdot [f_i]_{I,J} = [f_i]_{I,J+2} - 4[f_i]_{I,J+1} + 6[f_i]_{I,J} - 4[f_i]_{I,J-1} + [f_i]_{I,J-2}. \tag{2.13b}$$

2.3 Time marching

A modified, fifth order, Runge-Kutta time differencing scheme is used to advance the computations in time

$$f_i^{n+1} = f_i^n + \alpha_l \Delta f_i^{l-1}, \tag{2.14a}$$
$$\alpha_1 = 0.0695, \quad \alpha_2 = 0.1602, \quad \alpha_3 = 0.2898, \quad \alpha_4 = 0.5, \quad \alpha_5 = 1, \quad l = 1,2,\cdots,5. \tag{2.14b}$$

In the above equation n denotes the time step and

$$\Delta f_i^{l-1} = \frac{\Delta t \cdot (S_i^{l-1} + Q_i^{l-1})}{A_{I,J}}. \tag{2.15}$$

Therefore, the new-time particle distribution function is calculated as follows:

$$f_i^{n+1} = f_i^n + \alpha_l \frac{\Delta t}{A_{I,J}} (S_i^{l-1} + Q_i^{l-1}) \tag{2.16}$$

based on the CFL (Courant-Friedrichs-Lewy) criterion, the time step is given by:

$$\Delta t = CFL \times \left(\min \left(\sqrt{\Delta x_{I,J}^2 + \Delta y_{I,J}^2} \right) \right) \Big/ \left(\max \left(\sqrt{u_{I,J}^2 + v_{I,J}^2} \right) \right), \tag{2.17}$$

where the term CFL is set less than 0.7 for enhanced stability and $\Delta x_{I,J}$, $\Delta y_{I,J}$ are the projected lengths of the minimal area cell along the x and y directions, respectively.

2.4 Boundary conditions

One of the most critical issues of Lattice Boltzmann techniques is the implementation of the boundary conditions. In fact, the unknowns in the LBM are the particle distribution functions, while boundary conditions are defined as functions of the macroscopic fluid dynamics variables (i.e., velocity and pressure) or their derivatives. Therefore, boundary conditions must be defined in terms of the density distribution functions, while maintaining their physical meaning. Moreover, those well-established treatments of the boundary conditions used in the traditional BGK cannot be directly extended to finite volume formulations. In this section, various types of boundary conditions and their implementation with the present approach are discussed.

In order to transform hydrodynamic boundary conditions to the boundary conditions for the distribution functions, additional lattices at the edge of each boundary cell are introduced. Then, boundary nodes are treated like internal nodes, except that the fluxes over boundary edges also have to be evaluated.

As indicated in Fig. 2, physical boundaries of the computational domain are defined to be aligned with the lattice grid lines (on-grid formulation). The inlet boundary conditions at $I = 1$ are given by:

$$f_1 = f_3 + \frac{2u_{in}}{3}, \qquad f_5 = f_7 + 0.5(f_4 - f_2) + \frac{u_{in}}{6}, \qquad f_8 = f_6 + 0.5(f_2 - f_4) + \frac{u_{in}}{6}. \tag{2.18}$$
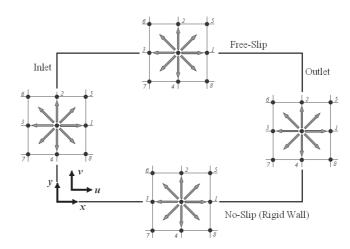
Figure 2: Physical boundaries of the solution domain and lattice model on typical boundaries.

The above described scheme is also known as Zou and He boundary conditions, suggesting the name of the original authors proposing this idea [23]. The other distribution functions are computed as follows:

$$f_i(I=1,J)=1.5f_i(I=2,J)-0.5f_i(I=3,J), \qquad i=0,2,3,4,6,7. \tag{2.19}$$

At the outlet boundary i.e., $I=N_x$, the distribution functions are extrapolated as follows [24,25]:

$$f_i(I=N_x,J)=1.5f_i(I=N_x,J)-0.5f_i(I=N_x-2,J). \tag{2.20}$$

Free-slip boundary conditions apply to the case of smooth boundaries with negligible friction exerted upon the flowing fluid. In this case, the tangential motion of the fluid flow on the boundary is free and no momentum is to be exchanged with the boundary along the tangential component. For free sleep boundary conditions (Fig. 2) the distribution functions are calculated as follows:

$$f_8=f_5, \qquad f_4=f_2, \qquad f_7=f_6. \tag{2.21}$$

This implies no tangential momentum transfer to the boundary, as required for a free sleep fluid motion. The condition $f_4=f_2$ implies that the component of the flow speed normal to the wall is null. The other distribution functions (i.e., $i=0,1,3,5,2,6$) are computed by extrapolation scheme.

Wall boundary conditions are in lattice Boltzmann simulations usually implemented by applying so-called bounce-back rule or no-slip boundary conditions in the case when a solid obstacle imposes friction (Fig. 3). During propagation, the component of the distribution function that would propagate into the solid node is bounced back and ends up back at the fluid node, but pointing in the opposite direction. This means that incoming
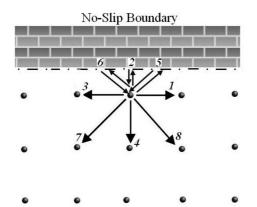
Figure 3: Schematic of bounce-back algorithm for straight wall.
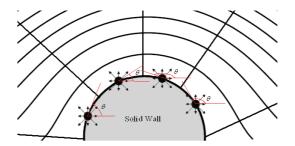

Figure 4: Schematic of complex wall.

particle portions are reflected back towards the nodes they came from. In this study the halfway bounce-back scheme is applied, which gives second-order accuracy for straight walls [24]:

$$f_6 = f_8, \qquad f_2 = f_4, \qquad f_5 = f_7. \tag{2.22}$$

As we mentioned before, the used scheme is capable to develop for unstructured rectangular meshes. On the arbitrary shaped solid walls (Fig. 4) we can apply the halfway bounce-back scheme [25]. The numerical results have shown that scheme has high accuracy for solid walls especially in the concave and convex corners [26]. For arbitrary shaped solid walls, the θ (Fig. 4) suggests the selection of appropriate f_i is for extrapolation purposes.

Periodic boundary condition can be used as inflow/outflow boundary conditions and is applied directly to the PDFs, and not to the macroscopic flow variables, which means the PDFs coming out of one boundary will enter into the opposite boundary. Periodic boundary conditions are applied to a boundary and a corresponding boundary counterpart.

Consider the domain illustrated in Fig. 2, a possible application of periodic boundary condition could be to link parallel the west boundary with the east one as well as the north with the south one.

The boundary values at the west end of the region $(x=0; y)$ are implemented by transferring the densities with positive x component of velocity from the east boundary $(x=nx; y)$:

$$f_{1,inlet}=f_{1,outlet}, \qquad f_{5,inlet}=f_{5,outlet}, \qquad f_{8,inlet}=f_{8,outlet}. \tag{2.23}$$

Note that it is only necessary to transfer three of the 9 densities that will then flow into the region.

3 Numerical viscosimeter

In order to measure the numerical viscosity, we simulate the evolution of the two-dimensional Taylor-Vortex flow in a square domain of width W and length L with periodic boundary conditions. The numerical results are compared to the analytical solution:

$$u(x,y)=-u_0\cos(p_1x)\sin(p_2y)\cdot e^{-v(p_1^2+p_2^2)}, \tag{3.1a}$$

$$v(x,y)=-u_0\sin(p_1x)\cos(p_2y)\cdot e^{-v(p_1^2+p_2^2)}. \tag{3.1b}$$

In the Taylor-Vortex flow, the vortex field will decay with exponential rate $-v(p_1^2+p_2^2)\cdot t$. In Eq. (2.23), v is the kinematics viscosity of the fluid and $p_1=0$, $p_2=2\pi/W$ are the wave numbers along x and y directions, respectively. The velocity u_0 was chosen to be 0.1 and we set the $W=10$, $c_s^2=1/3$ and time step $dt=\tau/2$. The computational domain is a $N_x\times N_y=50\times50$ regular mesh.

We have found from this simulation that for different values of relaxation time τ, the kinematics viscosity is equal to $v=c_s^2\tau=\tau/3$. Fig. 5(a) shows the comparison between numerical and analytical solutions for the Taylor-Vortex flow for two different values of the relaxation time. Also Fig. 5(b) shows the results at different times for $\tau=0.01$. As one can see the agreement between numerical and analytical results is very good.
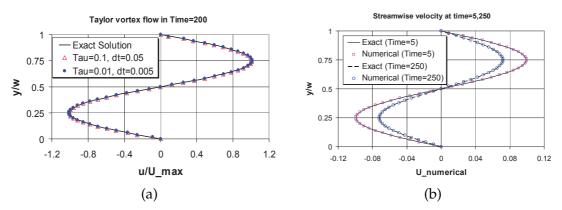

Figure 5: Analytical and calculated streamwise velocity profiles for the Taylor-Vortex flow simulation for $\tau=0.1, 0.01$ and time $t=5,250$.

Table 1: Numerical errors for the Taylor-Vortex flow ($t = 200$).

Time (t)	Iteration	$u_{exact\_maximum}$	$u_{numerical\_maximum}$	E_1
$\tau = 0.1$	4000	0.007194203	0.007219020	0.34%
$\tau = 0.01$	40000	0.076859628	0.077255092	0.51%

Table 2: Numerical viscosity error for the Taylor-Vortex flow in ($t = 200$, $\Delta t = \tau / 2$).

Time (t)	Calculated Viscosity	Numerical Viscosity Error (E_2)
$\tau = 0.1$	0.03328972	0.13%
$\tau = 0.01$	3.268E-03	1.96%

The numerical error relative to the exact solution, defined as $E_1 = |(u - u_{exact})/U_{max}| \times 100$, shown in Table 1. For this purpose, maximum error among all nodes of $x = w/2$ is calculated. Numerical viscosity error defined as $E_2 = (|v_{numerical} - v_{theoretical}|/v_{theoretical}) \times 100$ were also calculated. Results for different values of relaxation time are shown in Table 2.

4 Free shear flows simulation results

The computer code with the cell-centered FV-LBE formulation has been used to simulate three free shear flows namely 1-boundary layer flow over flat plate, 2-mixing layer and 3-free plane jet flow. The results are presented and discussed in this section.

As already mentioned, the present scheme could be applied to unstructured meshes too, but in this paper we limit our analysis to structured meshes with a regular rectangular tessellation. In this study, the computational domain is $L_x = L_y = 80\delta_{th}$, where δ_{th} is the theoretical thickness of the layer in $x = L_x$. This theoretical thickness is calculated
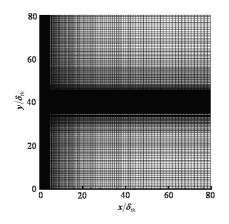

Figure 6: Used geometry in the jet/mixing layer flow simulation.

according to analytical solution for the boundary layer, flow and is estimated on the basis of the inlet velocity profile for jet and mixing layer flows. For the boundary layer flow $L_y = 40\delta_{th}$ has been chosen.

The computational domain employed for jet and mixing layer flows $(N_x \times N_y = 261 \times 521)$ is shown in Fig. 6. The center of the jet/mixing layer is located at $x_c = 0$ and $y_c = 40\delta_{th}$.

In the cross-stream direction y, an equally spaced grid is used in the jet/mixing layer vorticity thickness i.e., for $35\delta_{th} < y < 45\delta_{th}$, and then the grid is stretched on both sides. Also, in the stream-wise direction x, the grid is uniform between $0 < x < 5\delta_{th}$ and then stretched. A similar selection is used for the boundary layer flow.

4.1 Laminar boundary layer

Two dimensional boundary layer flow is a simple benchmark for flows with open, no-slip and free slip boundaries. Fig. 7 represents diagrammatically the velocity distribution in boundary layer and boundary conditions at the plate, with the dimensions across it considerably exaggerated. In front of the leading edge of the plate the velocity distribution is uniform. With increasing distance from the leading edge in the downstream direction, the thickness, δ, of the retarded layer increases continuously.

Fig. 8 shows a part of the computational domain and velocity vectors in which the LBE equations for the incompressible laminar boundary layer flow are solved. The results of the simulation display essentially laminar growth at the low Reynolds numbers.
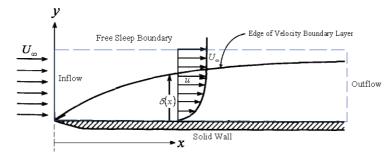

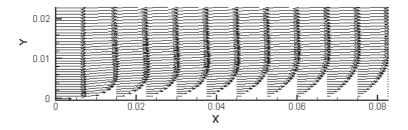Figure 7: Sketch of boundary layer on a flat plate.

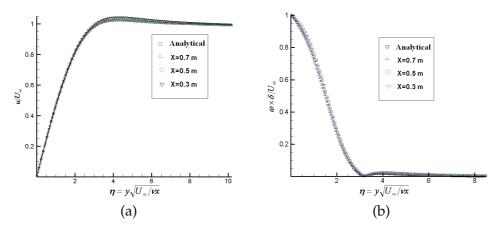Figure 8: Velocity vectors of boundary layer flow at $Re = 25$.

Figure 9: (a) Velocity and (b) vorticity distribution in the boundary layer along a flat plate.

Results in self-similar coordinate were also investigated. The mean field statistics for the streamwise velocity component are illustrated in Fig. 9(a) and compared with analytical solution of Blasius [27]. All quantities are non-dimensionalized by the appropriate characteristic scales of the flow. Specially, all lengths are normalized by the boundary layer thickness, δ and velocities are normalized by U_∞, where U_∞ is the free stream streamwise velocity. The vorticity component $\omega = \partial u/\partial y + \partial v/\partial x$ is also calculated. Fig. 9(b) shows the mean field statistics results of vorticity. Clearly, these results are representative of a self-similar layer. Fig. 10 shows the growth of the boundary layer thickness which has an excellent agreement with the analytical solution.
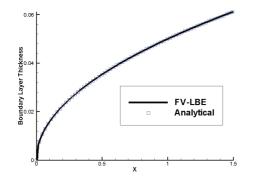

Figure 10: Growth of the boundary layer thickness.

4.2   Mixing layer

The plane mixing layer is characterized by the merging of two co-flowing fluid streams with different velocities. Typically, the two streams are separated by an impermeable object upstream of the confluence of these streams. The flow geometrical sketch is reported in Fig. 11. Downstream of the confluence, the two streams exchange momentum as they
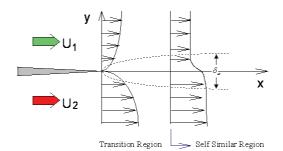
Figure 11: Schematic of plane mixing layer.

come into intimate contact with each other. The mixing layer itself is defined by the region in which this merging process is occurring. Being such a simple configuration, the mixing layer is one of the most common flows experienced in nature. Mixing layer are encountered in many application such as combustion furnaces, chemical lasers, the lip of an intake valve in an internal combustion engine and the trailing edge of a turbine blade.

In this flow, two initially unperturbed parallel flow streams with velocities U_1, U_2 interact each other as a consequence of friction from the position $x=0$ to downstream [27]. Due to the low viscosity, the transition from velocity U_1 to velocity U_2 takes place in a thin mixing zone, in which the transverse component v of the velocity is small if compared to the longitudinal velocity component u.

The flow is initially at rest (zero speed) and is impulsively started by forcing a hyperbolic profile such as $U_{inlet}(y)=0.5\{(1/\lambda)+\tanh(y)\}$ at inlet where $\lambda=[U_1-U_2]/[U_1+U_2]$ represents a measure for the intensity of the layer shearing. The flow has been numerically simulated for a Reynolds number equal to 300 defined as $Re_{\delta_{\omega 0}}=\Delta U\delta_{w0}/v$, being $\delta_{\omega 0}$ the vorticity thickness of the reference (inlet) velocity profile and $\Delta U=U_1-U_2$.

When the flow gets steady, the results of the simulation essentially display a laminar growth of the boundary layer. Fig. 12(a) illustrates the streamwise growth of the vorticity thickness, $\delta_\omega=1/(\partial\bar{U}/\partial y)_{\max}$ at $Re=300$. In this case, the average layer speed, $\bar{U}=0.5(U_1+U_2)$, is set at 1.5 in lattice units. A square-root relationship fit to these computed results is shown in the graph reported in Fig. 12(a). The layer is responded with the classical laminar, square-root growth characteristics [28]. This is evident by the close agreement indicated by the computed results. Fig. 12(b) shows velocity profiles for the mixing of the two uniform laminar streams at different velocities.

Results in self-similar coordinates for the mixing layer were also investigated. The principle of self similarity as a representation of moving equilibrium was introduced by Townsend [29]. Free shear layers provide an excellent example of this equilibrium, and they form one class of canonical laminar and turbulent flow fields. A dimensionless variable that is written as a function of a dimensionless transverse coordinate is called "self-similar" if the function does not change with the downstream position.

In order to verify our results, present numerical results are compared to the experimental data of Oster and Wygnanski [30]. Non-dimensional time-averaged streamwise
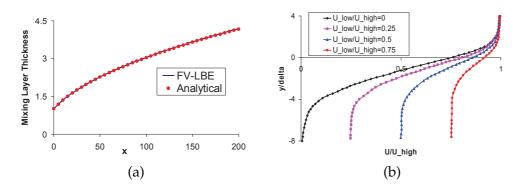
Figure 12: (a) Streamwise growth of the vorticity at $Re=300$. Curve fit using $\delta_\omega = 0.2875\sqrt{x+12.371}$ and (b) Velocity profiles for the mixing layers at different velocities.
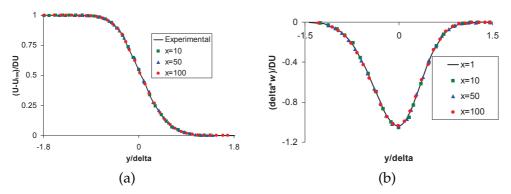

Figure 13: The cross-stream variation of the normalized (a) u-component velocity, (b) vorticity.

velocities and vorticities obtained by a statistical method at different stations are shown in Fig. 13. These results clearly show that self-similarity of the mixing layer is caught by the simulation and indicates that mixing layer is a flow with a self-preserving state. The quantitative agreement between numerical and experimental mean streamwise velocity and vorticity is satisfactory.

4.3 Jet flow

In this section, the simulation of a two-dimensional plane jet presented. A jet is formed by a flow issuing from a nozzle into an ambient fluid, which is at a different velocity. If the ambient fluid is at rest the jet is referred to as a "free jet"; if the surrounding fluid is moving, the jet is called a "co-flowing jet". A jet is one of the basic flow configurations which has many practical applications such as in jet engines, combustors, chemical lasers, ink-jet printer heads, among others. Fig. 14 illustrates features of a free jet flow.

In [27] it is shown that the layer thickness of a free jet flow grows and the local maximum velocity decays with the downstream distance as $x^{2/3}$ and $x^{-1/3}$, respectively, being x is the distance downstream from the jet nozzle.
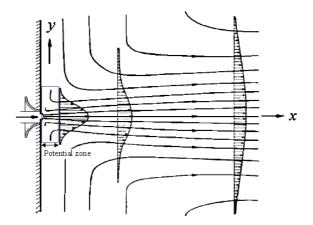
Figure 14: The laminar 2D free jet flow.

The central portion of the jet, a region with an almost uniform mean velocity, is called the "potential core". Because of the shear layer spreading, the potential core eventually disappears at a distance of about four to six diameters downstream from the nozzle. The entrainment process continues further beyond the end of the potential core region such that the velocity distribution of the jet eventually relaxes to an asymptotic bell-shaped velocity profile as illustrated in Fig. 14.

Here, we assume that the flow is initially at rest and is started by forcing a hyperbolic profile, $U_{inlet}(y) = 1/\cosh^2(y)$, after the potential core [27]. Moreover, the half-width of the jet, $\delta 1/2$, is defined as the distance between the axis and the location where the local velocity equals half of the local maximum or centerline velocity, U_m.

The increase in the jet half-width with the downstream distance provides a measure of the spreading rate of the jet. Fig. 15(a) shows the growth of the jet half width thickness at $Re = 300$. This thickness grew with the downstream distance as a function of $x^{2/3}$ and $\delta = 0.889(x+0.949)^{2/3}$ fit to these simulation results. Due to the spreading, the jet centerline velocity, U_m, decreases downstream beyond the potential core region. Fig. 15(b) illustrates the centerline velocity of the free jet which decays as $x^{-1/3}$. A curve fit to these computed results is shown in the graph of Fig. 15(b). This is evident by the close agreement indicated by the computed results.

The jet similarity characteristics in the transition process have been studied in [27] as well. The velocity profiles in various regions of the jet flow are plotted non-dimensionally and compared with analytical solutions in [27]. The streamwise mean velocity and vorticity distributions are presented in Fig. 16(a) and (b) respectively, where the velocities are normalized by the centerline velocity, and the jet discharging distance is normalized by the jet half-width thickness, shown as U/U_m and $y/\delta_{1/2}$, respectively. Fig. 16(a) presents mean velocity profiles measured at several streamwise locations in the jet. The collapse of the profiles in the similarity coordinates $U = U_M$ versus $y = \delta_{1/2}$ is clearly evident. Fig. 16(b) reports the normalized time averaged vorticity profiles at different stations.
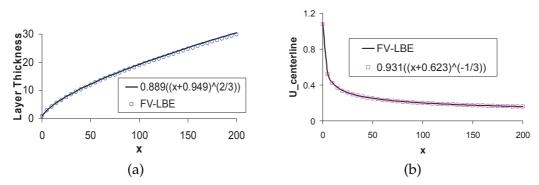
Figure 15: (a) Growth of the jet half-width, (b) decay of the centerline velocity of free jet.
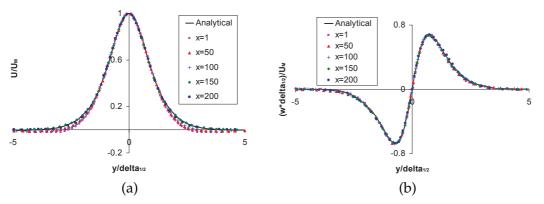

Figure 16: The cross-stream variation of the normalized (a) u-component velocity, (b) vorticity.

These figures show that the profiles express self-similarity at low Reynolds numbers. Most of the data could fit the analytical curve quite well, except very close to the jet inlet. A high degree of similarity is found in the downstream regions.

5 Uniform flow over 2D circular cylinder

The efficiency of the used scheme for curved boundaries was studied with reference to a uniform flow past a circular cylinder, that has been both numerically and experimentally studied extensively in the past, thus becoming a standard benchmark problem. The flow has been numerically simulated for Reynolds number ranging between 20 and 100. The Reynolds number is calculated as $Re = UD/v$, being U the inlet uniform velocity and D the cylinder diameter.

Fig. 17(a) shows a schematic of the flow configuration and boundary conditions that has been simulated here. The symmetry boundary conditions were used for top and bottom walls. All the simulations have been performed in a large $32D \times 16D$ domain so as to minimize the effects of the boundaries on the development of the wake. Grid
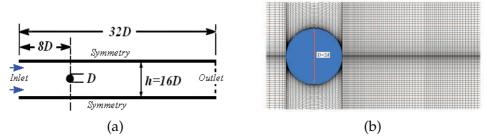
Figure 17: Flow configuration for simulation of flow past a cylinder placed symmetrically in a planar channel and (b) mesh grids around circular cylinder.
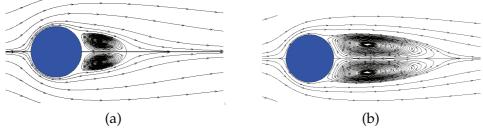

Figure 18: Streamlines at (a) $Re=20$ and (b) $Re=40$.

independence for non-dimensionalised wake length L was shown at $Re=30$ in Table 3. The 200×120 non-uniform mesh reported in Fig. 17(b) has been used in the present simulations for $Re=20$ and 40.

Table 3: Non-dimensionalised wake length versus grid size at $Re=30$.

Number of grids	120×70	150×80	180×100	200×120
L/d	2.88	3.06	3.1	3.1

The flow is impulsively started by forcing a uniform profile at inlet and after the fully periodic solution is reached, we measure and report the length of the wake behind the cylinder, the separation angle and the drag coefficient:

$$C_D = \frac{F_D}{(0.5\rho UD)},\tag{5.1}$$

where F_D is the drag force, which is the component of the aerodynamic force parallel to the free-stream velocity.

Details of the flow path behind the cylinder at the $Re=20$ and 40 are shown in Fig. 18. As expected the cylinder wake is steady and no vortex shedding is observed. Table 4 compares the present numerical results with previous experimental and computational results [31–39]. In particular the length of the wake behind the cylinder, the separation angle and the drag coefficient computed with the present method are in good agreement with the correspondent values available in literature.

Table 4: Comparison of geometrical and dynamical parameters: $L =$ length of wake, $d =$ cylinder radius, $\theta_s =$ separation angle.

Re	Authors	L/d	θ_s	C_D
20	Coutanceau and Bouard [31]	1.86	44.8	–
	Dennis and Chang [32]	1.88	43.7	2.045
	Nieuwstadt and Keller [33]	1.786	43.37	2.053
	He and Doolen [34]	1.842	42.96	2.152
	Patil and Lakshmisha [35]	1.884	42.81	1.949
	Fornberg [36]	1.82	–	2
	Calhoun [37]	1.82	–	2.19
	Ye et al. [38]	1.84	–	2.03
	Ubertini et al. [39]	–	–	2.09
	Present	1.82	42.5	2.205
40	Coutanceau and Bouard [31]	4.26	53.5	–
	Dennis and Chang [32]	4.69	53.8	1.552
	Nieuwstadt and Keller [33]	4.357	53.34	1.550
	He and Doolen [34]	4.49	52.84	1.499
	Patil and Lakshmisha [35]	4.284	52.74	1.558
	Fornberg [36]	4.48	–	1.5
	Calhoun [37]	2.18	–	1.62
	Ye et al. [38]	2.27	–	1.52
	Ubertini et al. [39]	–	–	1.56
	Present	4.47	52.8	1.551

Table 5: Comparison of Strouhal number and drag coefficient for unsteady flow at $Re = 100$.

Authors	Strouhal Number	C_D
Calhoun [37]	–	1.33
Ding et al. [40]	0.166	1.391
Liu et al. [41]	0.164	1.350
Braza et al. [42]	–	1.364
Present	0.161	1.310

It is generally accepted that the wake of a cylinder immersed in a free-stream first becomes unstable to perturbations at a critical Reynolds number of about $Re = 46 \pm 1$ see [38]. Above this Reynolds number, a small asymmetric perturbation in the near wake will grow in time and lead to an unsteady wake and Von Karman vortex shedding. This is indeed what we find for our simulation at $Re = 62$ which has been carried out on a 320×240 non-uniform mesh with a structure similar to the grid shown in Fig. 17(b).

Fig. 19(a) shows the behavior of residual of velocities (Eq. (3.1)) at $Re = 60, 65$ and 100. Also Fig. 19(b) shows the variation of drag coefficient with time at $Re = 100$ and it shows how vortex shedding develops to a periodic state in time.

The vortex shedding Strouhal number defined as $S_t = f_s D / U$, where f_s is the shedding frequency, is one of the key quantities that characterizes the vortex shedding process.
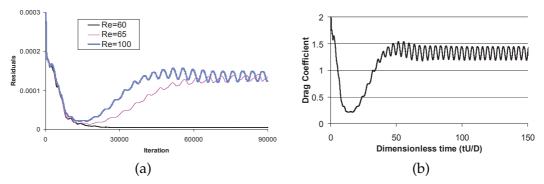
Figure 19: (a) Behavior of velocities residuals at $Re=60$, 65 and 100 and (b) variation of drag coefficient with time at $Re=100$.
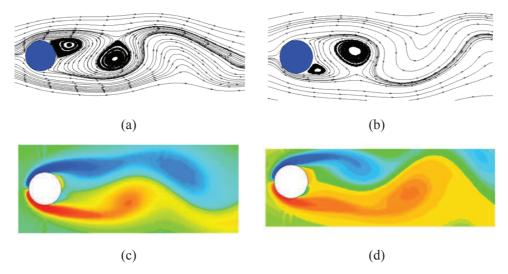

Figure 20: Plot of streamlines (a, b) and vorticity (c, d) at two times for $Re=100$.

Here we have estimated the Strouhal number from the periodic variation of the drag coefficient. Table 5 lists the quantitative comparisons for the Strouhal number, as well as the drag coefficient. Fig. 20 shows a plot of the streamline pattern and spanwise vorticity contour at two times instant for $Re=100$. Clearly, plots show the classical Karman vortex street.

6 Conclusions

This paper presents an accurate and stable cell-centered finite-volume formulation of the D2Q9 lattice Boltzmann equation with single time relaxation. An upwind scheme based on a least squares linear reconstruction of the populations in each control volume and upwind-biased second-order pressure-based flux weighting factors are used. In flux

modeling, we added an artificial dissipation to damp out the spurious oscillations, to increases the stability and accuracy of the numerical scheme. Boundary treatments have been extensively described. Time marching is performed through a fifth-order Runge Kutta method.

It has been provided numerical evidence that the corresponding kinematic shear viscosity is related to the relaxation time by $v = c_s^2 \tau$, with small numerical viscosity. Then some numerical tests against well-known free shear flow problems are presented to ensure the validity of the proposed numerical method. Namely a boundary layer flow over flat plate, a mixing layer flow and a free plane jet flow are simulated. An excellent agreement between present results and analytical solutions is observed, as well as the capability of the method to reveal the self-similar property of free shear layers.

Finally, the numerical procedure is applied to a uniform flow past a circular cylinder. This test enables to highlight the potentiality of a finite volume method with respect to traditional LBM, as grid refinement can be performed close to the body. Moreover, the simulation could be successfully performed also for unsteady flow, at $Re = 100$, where numerical instability was experienced by other finite volume formulations available in literature.

References

[1] P. L. Bhatnagar, E. P. Gross and M. Krook, A model for collision processes in gases I: small amplitude processes in charged and neutral one component systems, Phys. Rev., 94 (1954), 511.

[2] Y. Qian, D. d'Humie'res and P. Lallemand, Lattice BGK models for Navier-Stokes equation, Europhys. Lett., 17 (1992), 479.

[3] J. P. Rivet and J. P. Boon, Lattice Gas Hydrodynamics, Cambridge University Press, 2000.

[4] R. Benzi, S. Succi and M. Vergassola, The lattice Boltzmann equation: theory and applications, Phys. Rep., 222 (1992), 145.

[5] B. M. Boghosian, F. J. Alexander and P. Coveney, Proceedings of conference on discrete models for fluid mechanics, Int. J. Mod. Phys. C, 8(4) (1997), 637.

[6] S. Chen and G. D. Doolen, Lattice Boltzmann method for fluid flows, Ann. Rev. Fluid Mech., 30 (1998), 329.

[7] G. Falcucci, S. Ubertini, C. Biscarini, S. Di Francesco, D. Chiappini, S. Palpacelli, A. De Maio and S. Succi, Lattice Boltzmann methods for multiphase flow simulations across scales, Commun. Comput. Phys., 9 (2011), 269–296.

[8] D. Chiappini, G. Bella, S. Succi, F. Toschi and S. Ubertini, Improved lattice Boltzmann without parasitic currents for Rayleigh-Taylor instability, Commun. Comput. Phys., 7 (2010), 423–444.

[9] S. Succi, The Lattice Boltzmann Equation for Fluid Dynamics and Beyond, Oxford University Press, 2001.

[10] D. A. Wolf-Gladrow, Lattice-Gas Cellular Automata and Lattice Boltzmann Models: An Introduction, Springer, 2000.

[11] X. He, L. S. Luo and M. Dembo, Some progress in lattice Boltzmann method: part I: nonuniform mesh grids, J. Comput. Phys., 129 (1996), 357.

[12] F. Nannelli and S. Succi, The lattice Boltzmann equation on irregular lattices, J. Stat. Phys., 68 (1992), 401.

[13] G. Peng, H. Xi, C. Duncan and S. H. Chou, Finite volume scheme for the lattice Boltzmann method on unstructured meshes, Phys. Rev. E, 59 (1999), 4675.

[14] H. Xi, G. Peng and S. H. Chou, Finite volume lattice Boltzmann method, Phys. Rev. E, 59 (1999), 6202.

[15] S. Ubertini, S. Succi and G. Bella, Lattice Boltzmann method on unstructured grids: further developments, Phys. Rev. E, 68 (2003), 016701.

[16] M. Stiebler, J. Tolke and M. Krafczyk, An upwind discretization scheme for the finite volume lattice Boltzmann method, Comput. Fluids, 35 (2006), 814.

[17] H. Chen, Volumetric formulation of the lattice Boltzmann method for fluid dynamics: basic concept, Phys. Rev. E, 58 (1998), 3955.

[18] S. Ubertini and S. Succi, Recent advances of Lattice Boltzmann techniques on unstructured grids, Prog. Comput. Fluid Dyn., 5 (2005), 85.

[19] S. Ubertini and S. Succi, A generalised lattice Boltzmann equation on unstructured grids, Commun. Comput. Phys., 3 (2008), 342.

[20] C. Hirsch, Numerical Computation of Internal and External Flows, Vol. I: Fundamentals of Numerical Discretization, Wiley, 1988.

[21] J. Ghasemi and S. E. Razavi, On the finite volume lattice boltzmann modeling of thermo-hydrodynamics, Comput. Math. Appl., 60 (2010), 1135.

[22] J. C. Tanehill, D. A Anderson and R. H. Pletcher, Computational Fluid Mechanics and Heat Transfer, Taylor & Francis, 1997.

[23] Q. Zou and X. He, On pressure and velocity boundary conditions for the lattice Boltzmann BGK model, Phys. Fluids, 9 (1997), 1591.

[24] S. Chen, D. Martinez and R. Mei, On boundary conditions in lattice Boltzmann methods, Phys. Fluids, 8 (1996), 2527.

[25] Z. Guo, C. Zheng and B. Shi, An extrapolation method for boundary conditions in lattice Boltzmann method, Phys. Fluids, 14 (2007), 2002.

[26] B. Chopard and A. Dupuis, A mass conserving boundary condition for lattice Boltzmann models, Int. J. Mod. Phys. B, 17 (2003), 103.

[27] H. Schlichting, Boundary Layer Theory, Springer, 2005.

[28] P. S. Lowery and W. Reynolds, Numerical simulation of spatially developing forced plane mixing layer, NASA Technical Report NCC2-015, 1986.

[29] A. A. R. Townsend, The Structure of Turbulent Shear Flow, Cambridge University Press, 1956.

[30] D. Oster and I. Wygnanski, The forced mixing layer between paralell streams, J. Fluid Mech., 123 (1982), 91.

[31] M. Coutanceau and R. Bouard, Experimental determination of the main features of the viscous flow in the wake of a circular cylinder in uniform translation: part 1: steady flow, part 2: unsteady flow, J. Fluid Mech., 79 (1977), 231.

[32] S. C. R. Dennis and G. Z. Chang, Numerical solutions for steady flow past a circular cylinder at Reynolds numbers up to 100, J. Fluid Mech., 42 (1970), 471.

[33] F. Nieuwstadt and H. B. Keller, Viscous flow past circular cylinders, Comput. Fluids, 1 (1973), 59.

[34] X. He and G. Doolen, Lattice Boltzmann method on curvilinear coordinates system: flow around a circular cylinder, J. Comput. Phys., 134 (1997), 306.

[35] D. V. Patil and K. N. Lakshmisha, Finite volume TVD formulation of lattice Boltzmann sim-

ulation on unstructured mesh, J. Comput. Phys., 228 (2009), 5262.

[36] B. Fornberg, A numerical study of steady viscous flow past a ircular cylinder, J. Fluid Mech., 98 (1980), 819.

[37] D. Calhoun, A cartesian grid method for solving the two-dimensional streamfunction-vorticity equations in irregular regions, J. Comput. Phys., 176 (2002), 231.

[38] T. Ye, R. Mittal, H. Udaykumar and W. Shyy, An accurate cartesian grid method for viscous incompressible flow with complex immersed boundaries, J. Comput.l Phys. 156 (1999), 209.

[39] S. Ubertini, S. Succi and G. Bella, Lattice Boltzmann Scheme without Coordinates, Phil. Trans. R. Soc. Lond. A, 362 (2004), 1763.

[40] H. Ding, M. Shu and Q. D. Cai, Application of stencil-adaptive finite difference method to incompressible viscous flows with curved boundary, Comput. Fluids, 36 (2007), 786.

[41] C. Liu, X. Zheng and S. H. Sung, Preconditioned multi-grid methods for unsteady incompressible flows, J. Comput. Phys., 139 (1998), 35.

[42] M. Braza, P. Chassaing, and H. Ha Minh, Numerical study and physical analysis of the pressure and velocity fields in the near wake of a circular cylinder, J. Fluid Mech., 165 (1986), 79.